Energy & Environmental Science

ROYAL SOCIETY OF CHEMISTRY

PAPER

View Article Online
View Journal | View Issue

Cite this: *Energy Environ. Sci.*, 2025, **18**, 674

Long term outdoor performance evaluation of printed semitransparent organic photovoltaic modules for BIPV/BAPV applications†

Sarmad Feroze, *[a] Andreas Distler, [a] Lirong Dong, [a] Michael Wagner, [b] Iftikhar Ahmed Channa, [c] Felix Hoga,[d] Christoph J. Brabec*[ab] and Hans-Joachim Egelhaaf[ab]

Recently, organic photovoltaics (OPV) have achieved power conversion efficiencies (PCE) above 20% thus coming closer to market entry. Building-integrated photovoltaics (BIPV) and building-attached photovoltaics (BAPV) are two key areas where the functional advantages of both OPV and BIPV/BAPV complement each other and thus could pave the way for market penetration of OPV. Herein, we report on large-area, all-solution-processed flexible OPV modules manufactured by a fully roll-to-roll (R2R) method with high levels of process repeatability. The OPV modules show an accelerated lifetime (ALT) of more than 1000 h and 2800 h under the ISOS-L2 and ISOS-D3 testing conditions, respectively. Long-term outdoor monitoring of the OPV modules was conducted in a typical central European climate, considering two distinct mounting angles that hold significant relevance for BIPV installations *i.e.*, 45° inclination with respect to the ground (representing the optimal tilt angle of the site) and 90° vertical mounting (as mostly encountered in BIPV façades). The ISOS-O2 protocol was used as the test standard for outdoor monitoring. The results show that the OPV modules can offer higher daily specific energy yields (Y_{FD}), *i.e.*, higher ratios of daily energy yield and STC W_P capacity of the module, than a reference mono-crystalline (m-Si) module for BIPV installations typical of a rooftop case (*i.e.*, 45°), whereas for façade integrated cases (*i.e.*, 90°), OPV modules offer Y_{FD} values identical to that of m-Si modules. Detailed laboratory investigations reveal that the higher Y_{FD} values of the OPV modules at 45° mounting stems from their negligible temperature coefficient of −0.008% °C^{-1}, whereas at 90° mounting, the angle-dependent response of the modules plays a crucial role.

Received 5th September 2024,
Accepted 29th November 2024

DOI: 10.1039/d4ee04036h

rsc.li/ees

Broader context

Organic photovoltaics (OPV) have the potential to fill niches that traditional silicon photovoltaics (Si-PV) have left open so far. Building-integrated and building-attached photovoltaics (BIPV/BAPV) highlight OPV's functional advantages, especially in land-efficient applications. Our study investigates the outdoor energy harvesting capabilities of flexible semi-transparent OPV modules manufactured in a fully solution-processed route using high-throughput roll-to-roll (R2R) printing methods. We demonstrate that OPV can offer higher ratios of daily energy yield to STC W_P capacity of the module, than a reference m-Si module for BIPV installations typical of a rooftop case (*i.e.*, 45°), whereas for façade integrated cases (*i.e.*, 90°), OPV modules offer daily specific energy yields values identical to that of m-Si modules. We demonstrate that the higher specific yield of the OPV modules can be quantitatively explained based on their indoor characteristics (light, angle, and temperature dependence). By considering the indoor angle, light, and temperature-dependent response of both module types, the energy harvest predictions achieved a precision of ±5%. Finally, the systematic modifications of HTL thickness and donor acceptor ratio in the photoactive layer, the module lifetime was enhanced to 1000 h and 2800 h, as monitored in ALT according to ISOS-L2 and ISOS-D3 standards respectively.

[a] *Institute of Materials for Electronics and Energy Technology (i-MEET), Faculty of Engineering, Department of Material Science, Friedrich-Alexander-Universität Erlangen-Nürnberg (FAU), 91058 Erlangen, Germany.*
E-mail: sarmad.feroze@fau.de, christoph.brabec@fau.de
[b] *Helmholtz-Institut Erlangen-Nürnberg für Erneuerbare Energien (IEK-11), Forschungszentrum Jülich GmbH, 91058 Erlangen, Germany*
[c] *Department of Materials and Metallurgical Engineering, NED University of Engineering and Technology, 75270 Karachi, Pakistan*
[d] *Automatic Research GmbH, Paniersplatz 13, 90403 Nürnberg, Germany*

† Electronic supplementary information (ESI) available. See DOI: https://doi.org/10.1039/d4ee04036h

1. Introduction

Organic photovoltaics (OPV) are often considered as the next-generation photovoltaic (PV) technology due to their functional attributes of semi-transparency, flexibility, low production cost, and short energy payback times.[1–5] These unique features allow OPV to offer applications ranging from portable device charging to complex building-integrated photovoltaics (BIPV) and

building-attached photovoltaics (BAPV) systems, with the latter being considered the two most promising contenders for real-world applications.[6] During the last decade, significant progress in high-performance polymers and the advent of non-fullerene acceptors (NFAs) have enabled OPV to surpass the power conversion efficiency (PCE) benchmarks of 20% and 14% for small research cells and sub-modules (200–800 cm^2) respectively.[7–9] Furthermore, OPV has demonstrated cost competitiveness with established PV technologies.[10,11] However, despite such rapid progress in device efficiencies, the exploitation of the functional advantages offered by OPV is still far from reality. On one hand, this is due to the challenges of cost-effective upscaling of OPV module production by fully solution-processed roll-to-roll (R2R) methods. Despite the existence of literature reports on high-performance photoactive layers (PAL) systems used in OPV module fabrication, these systems still require the use of vacuum-deposited metal oxides as hole transport layers (HTL) and vacuum-deposited metal top electrodes to achieve full module performance. Consequently, the application of these systems in fully R2R-compatible OPV module manufacturing is hindered.[8,12,13] On the other hand, the incorporation of OPV modules into large-scale BAPV or BIPV systems is influenced, at least in part, by the limited understanding of the longevity and performance of OPV modules under actual operational conditions. While efficiency and cost are generally acknowledged as the two important metrics for the commercialization of any PV technology, long operational lifetimes are equally important for practical applications, a benchmark that remains a challenge for OPV. Well-known mechanisms in OPV device degradation include photo and oxygen-induced degradation of the PAL, instability of charge transport layers (CTL) and electrodes, interface-related degradation, and device encapsulation failures.[14] The majority of the lifetime studies reported in literature have been conducted on small lab-scale cells where the devices are kept under well-controlled and fixed laboratory conditions, with various studies reporting device lifetimes ranging from a few hours to several thousand hours.[15–19] However, such indoor lifetimes cannot guarantee smooth device operation under actual outdoor conditions where they always operate under dynamic environmental stresses and at maximum power point (MPP) conditions. This emphasizes the importance of outdoor field testing, which is considered a vital step in the commercialization of OPV.

For commercial success, OPV needs to look for niche markets and one such area is BIPV/BAPV, where the functional attributes of OPV and land-free PV application of BIPV/BAPV complement each other.[20] In BIPV systems, the PV modules are integrated into building materials such as roof elements, windows, and facades, whereas in BAPV, the PV modules are retrofitted/attached to an existing building envelope. In a basic BAPV configuration, OPV modules can be deployed on the roofs and walls of, *e.g.*, storage buildings. Given that these structures are generally not designed to accommodate substantial loads, the lightweight characteristics of OPVs, which weigh significantly less than 1 kg m^{-2}, render them more suitable than crystalline silicon modules, which are approximately ten times heavier.[21] The OPV modules can be fixed with double-sided adhesive tape, which provides them with a simple advantage over other options. Since these industrial structures are only intended to last for a few years the limited lifespan of OPV is not a major concern. Similarly, the ability of BIPV to seamlessly blend into the building envelope offers an aesthetic advantage that appeals to architects, builders, and property owners alike. OPV are highly suitable for applications in glass facades and windows because of their ability to achieve semitransparency with reasonable losses while maintaining color-neutral absorption, which sets them apart from traditional PV technologies.[22,23] In addition to its primary function of generating electricity, BIPV/BAPV can offer several other practical benefits to buildings, including weather protection, thermal insulation, noise reduction, and electromagnetic shielding, and has the potential to reverse the status of buildings from energy consumers to energy producers.[24] The market value of the BIPV sector was estimated to be €2.7 billion in 2015, with an observed compound annual growth rate of 11.0% from 2012 to 2014,[25] and is estimated to reach €30 billion in the coming years.[20] In a more recent study, the OPV market is valued at approximately $1.75 billion as of 2023, and is forecast to grow significantly, reaching $12.93 billion by 2032, with the BIPV segment expected to account for 32% of the total market share.[26] However, determining the global BIPV/BAPV potential is challenging because of the difficulty in accurately estimating the total surface areas suitable for these applications. According to a study conducted by the International Energy Agency (IEA), the total area that could be utilized for such applications reaches approximately 230 billion m^2 globally and could potentially meet 11% of the world's electricity demand by 2050. Clearly, the above statistical data indicates that the potential of BIPV/BAPV is far from being exhausted and thus emphasizes the importance of high-throughput methods that can achieve these PV expansion and production goals within reasonable timeframe.

In almost all BIPV/BAPV systems the PV modules are installed at a fixed non-optimal inclination angle because of the architectural constraints of the building and are therefore seldom irradiated at normal angles of incidence. Parameters such as light intensity, spectral distribution of solar irradiance, module temperature (T_{MOD}), and angle of incidence at which the solar irradiation is received by the module play an important role in the electrical performance of any PV type. However, for OPV, there is a paucity of published data on their PV behavior under real-world outdoor operating conditions, particularly about their long-term outdoor performance evaluation.[27,28] A few studies show that OPVs hold performance advantages in terms of their superior temperature coefficient, oblique angle, and low-light performance; the conditions that are very obvious for most BIPV/BAPV installations.[25,29–33] However, comparative outdoor investigations that analyze the effect of the above three parameters on the long-term outdoor energy harvest of OPV within the context of BIPV/BAPV installation are very limited. Also, there are no defined regulations to establish the experimental conditions for the outdoor testing procedures of OPV, especially within the framework of BIPV/BAPV. The closest approach is the ISOS-O protocol, in which three different outdoor testing conditions are defined: basic, intermediate, and advanced levels that provide detailed

instructions for outdoor data reporting.[34] One such recommendation pertains to the presentation of degradation curves for the normalized PCE. It is advisable to gather data exclusively under irradiances ranging from 800 to 1000 W m^{-2} to minimize the occurrence of nonlinear effects that may arise outside this range. However, it is essential to acknowledge that certain requirements outlined in the protocol may not be applicable or easily achievable when integrating BIPV/BAPV devices. For example, encountering irradiances above 800 W m^{-2} or implementing module inclination at a latitude angle/tracking can present challenges.

In a prior study conducted by our research group, an investigation was undertaken to analyze the outdoor energy harvest of the first generation of commercially available OPV and compare it to that obtained with m-Si modules for a period of one month during summer, with the aim of evaluating performance of both module technologies within the context of BIPV configuration.[33] In this work, we report on the outdoor energy harvest of flexible semi-transparent OPV modules manufactured in a solution-processed route using high-throughput R2R methods. All the functional layers of the OPV modules were deposited onto laser patterned poly(ethyleneterephthalate) (PET)/indium tin oxide (ITO)/Metal/ITO (IMI) flexible substrates by an industrial-scale slot-die coating technique, using only commercially available materials (see Section 4 for details). For the PAL, the P3HT:o-IDTBR donor–acceptor system was used. The complete cell stack structure used for OPV module manufacturing, and the module layout are shown in Fig. S1 and S2 (ESI†) respectively. The choice of using this PAL system is due to its decent efficiency and lifetime demonstrated in the literature at research cell level and its easy upscaling to module level using industry-compatible solution processing methods.[35–39] The resulting OPV modules are characterized by noteworthy efficiencies, commendable operational lifetimes, and robust module manufacturing processes. The outdoor energy harvest investigations of the manufactured modules are carried out over a full calendar year, providing insights into the energy harvesting capabilities of both OPV and m-Si modules. The analysis takes into consideration the diverse seasonal variations observed throughout the annual cycle.

First, the angle-dependent, light-dependent, and temperature-dependent PV responses of both OPV and m-Si modules were investigated under laboratory conditions. Afterwards, the long-term outdoor monitoring of the modules was conducted for a typical central European climatic condition using ISOS-O2 as a testing standard. In the context of outdoor monitoring, the energy harvesting of OPV modules is investigated for two different module inclinations, where they tend to have the highest potential for practical installations, namely (1) the optimal tilt angle of the site as per ISOS-O2 recommendations, that is, the front side oriented towards the south at the site latitude angle (as mostly encountered for a rooftop installation), and (2) for a south-faced vertical BIPV facade orientation (90° with respect to the horizontal axis). For a comparative analysis, the energy harvest of the OPV modules was benchmarked against a commercial monocrystalline silicon (m-Si) module. The recorded energy harvest was then compared with a simulated energy harvest. The simulation employs a model that uses the three laboratory investigations mentioned above (angle dependence, light dependence, and temperature dependence) to predict the energy harvest of both module types for the outdoor operating conditions observed during outdoor monitoring and tracks outdoor module degradation. In order to understand the outdoor degradation pattern and its influence on the recorded energy harvest of the OPV modules they were subjected to accelerated lifetime testing (ALT) under damp heat and continuous light-soaking conditions using ISOS-D3 (65 °C module temperature and 85%RH) and ISOS-L2 (1000 W m^{-2} light intensity and 65 °C module temperature) as test standards.[34]

2. Results and discussion

2.1. Laboratory investigations

2.1.1. Angle and light-intensity dependence. First, the initial performance (t_0) of the OPV modules was measured under STC (25 °C module temperature, 1000 W m^{-2} light intensity, and AM1.5G spectrum) as shown in Fig. S3 (ESI†). The results show very high levels of process repeatability and R2R production yield of >95%. The flexible OPV modules showed excellent mechanical flexibility when exposed to bending tests with bending radii of 5 cm and 2.5 cm respectively, with modules retaining their t_0 PCE after being subjected to 25 000 bending cycles (Fig. S4, ESI†).

To better understand the outdoor data, first the light intensity dependence and angle-dependent performance of the OPV modules (batch_A, see Section 4 for details) and of the m-Si modules were investigated under laboratory conditions. The angle-dependent and light-dependent characterizations of both module types were performed using a flasher light source (Endeas, QuickSun). For angle dependence, *I–V* curves were measured for every 5° angle increment at a constant module temperature of 25 °C. The module angle was varied from 0° to 80° between the surface normal of the module and the direction of the flasher with an accuracy of ±1° (Fig. S5, ESI†). For investigation of light intensity dependence, *I–V* characterizations were performed at a normal angle of incidence with respect to the light source at a constant module temperature of 25 °C. The light intensity varied between 1000 W m^{-2} and 94 W m^{-2} using density-neutral filters. Both laboratory investigations were benchmarked against a commercial m-Si module as a reference. Before the measurements, the encapsulated OPV modules were light-soaked for 30 minutes under 1000 W m^{-2} light intensity to achieve maximum performance. OPV devices incorporating metal oxides as ETL experience performance improvements under light exposure over time. This is due to the increasing conductivity of the ETL under illumination with UV light, which enhances the FF (Fig. S6, ESI†). This effect as well as potential countermeasures has been well documented in literature and is referred to as "light soaking effect".[40–42] In our case, the solution to reduce the light soaking time before the t_0 measurement was the direct exposure of the OPV modules to the UV light for 2–3 minutes to achieve the full module performance.

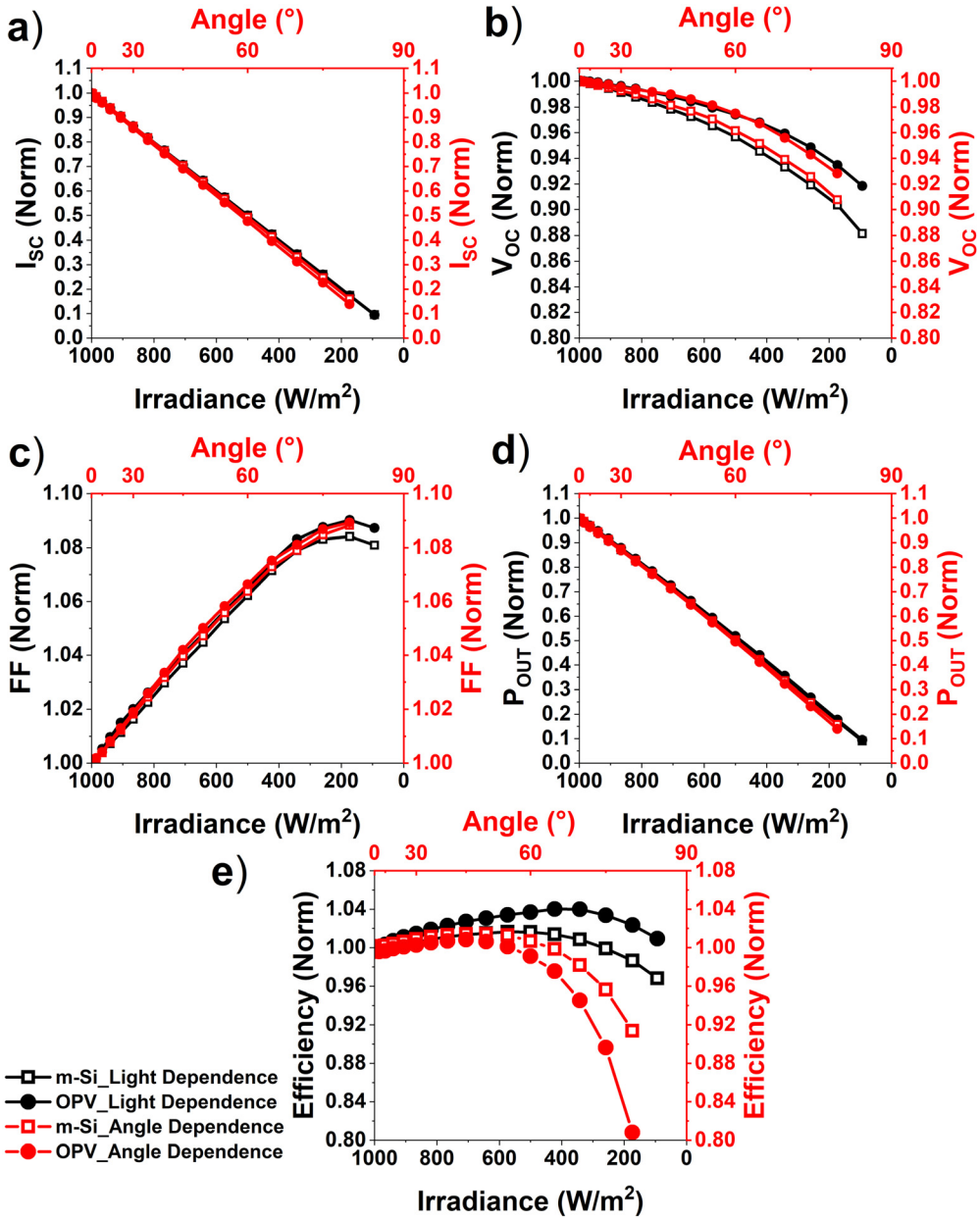

Fig. 1 Normalized key electrical parameters of both OPV and m-Si modules as extracted from the angle-dependent and light-dependent *I*–*V* characteristics of both module types made at a constant module temperature of 25 °C. The values are normalized at 1000 W m^{-2} and 0° for light dependent and angle dependent characterizations respectively. (a) Short-circuit current (I_{SC}), (b) open-circuit voltage (V_{OC}), (c) fill factor (FF), (d) power output (P_{OUT}) and (e) power conversion efficiency (PCE). The *x*-axis for angle-dependent characterization is scaled to $\cos(\theta)\pi/(180°)$ and the effective PCE is calculated with respect to the actual light intensity hitting the module surface at tilt angles following the Lambert cosine effect.

Fig. 1 summarizes the normalized key electrical parameters of both OPV and m-Si modules as obtained from their respective angle-dependent and light-dependent *I*–*V* characterizations (Tables S1 and S2, ESI†). Upon decreasing the intensity of the irradiated light from 1000 W m^{-2} to around 300 W m^{-2}, the PCE of the OPV modules increases by about 4%, due to the increasing FF (Fig. 1(c)), and then slightly decreases again upon further decreasing the incident light intensity, mainly due to the decreasing V_{OC} (Fig. 1(b)). The PCE of the m-Si module also increases with decreasing light intensity, however by approximately 2% at the maximum, which is reached at around 500 W m^{-2}. For lower light intensities, the PCE drops significantly. Thus, with respect to the light intensity of 1000 W m^{-2}, the OPV modules show relatively smaller drops of PCE than the m-Si module at all lower light intensities. At the lowest measured light intensity of 94 W m^{-2}, the relative PCE advantage of the OPV module over the m-Si module amounts to around 4%. For determining the angle dependence of module performance (Fig. 1), the effective PCE of both module types is calculated using the Lambert cosine effect, which considers the actual power of light incident onto the module

surface at a given angle.[43] Both module types show a relatively weak angle dependence of their PCE up to angles of incidence of around 50°, whereas the PCE drops significantly for angles larger than 60°. The PCE of the OPV module increases by around 1% of the value at normal incidence up to an angle of 45° and later drops for larger angles, down to 81% at an angle of incidence of 80°. For the m-Si module, a maximum PCE is observed at around 50°, which is approximately 2% higher than the PCE observed at 0°. At an angle of incidence of 80°, the PCE of the m-Si module reaches 91% of the value at normal incidence. The unfavorable angle-dependence of the OPV module arises due to short-circuit current (I_{SC}) limitations, especially at tilt angles greater than 45°, which is attributed to the amplified reflection of the s-polarized component of the incident light arising at the module encapsulation and air interface, thus limiting the in-coupling of the light (Fig. 1(a)).[25] Similar to the OPV module, the m-Si module also shows a similar reduction in I_{SC} with increasing angle of incidence arising from the reflection of incident light at the module and air interface (Fig. 1(a)). However, this effect is mitigated to some extent in the m-Si modules by using anti-reflection coating (ARC),[44] the exact nature of which has not been disclosed by the manufacturer.

2.1.2. Temperature dependence. To determine the temperature coefficient and possible temperature-induced irreversibility, temperature-dependent electrical characterizations were performed for the OPV modules (batch_B, see Section 4 for details). For this purpose, the module temperature T_{MOD} was elevated from 25 °C to 70 °C (±1 °C temperature tolerance) and then decreased from 70 °C to 25 °C (±1 °C temperature tolerance) in steps of 5 °C, using a hotplate as the heating source. The module was exposed to the respective temperatures for at least 5 min before measuring the *I–V* curves using an AAA-class solar simulator (Fig. S7, ESI†). Fig. 2 shows the temperature-dependence of the key PV performance indicators. For increasing module temperature, the OPV module shows a positive temperature coefficient for J_{SC} of approximately $\alpha = +0.004\%\ °C^{-1}$, while a linear drop in V_{OC} is observed, resulting in a negative temperature coefficient for V_{OC} for the given temperature range, $\beta = -0.014\%\ °C^{-1}$. The FF of the module remains relatively stable up to 50 °C, whereas a linear drop in FF is observed beyond this point. Overall, the OPV module exhibits a negative temperature coefficient for PCE ($\gamma = -0.008\%\ °C^{-1}$) in the temperature range of 25–50 °C and increases to $\gamma = -0.019\%\ °C^{-1}$ from 50 °C onwards, the cause of which is the additional FF loss at $T_{MOD} > 50$ °C. Compared to the temperature coefficients of the m-Si modules (Table 1), the temperature dependence of the OPV module performance is thus almost negligible. This is a consequence of the organic bulk heterojunction representing a disordered semiconductor, which leads to enhanced charge carrier mobility with increasing temperature and thus to reduced charge carrier recombination, which partly compensates for the decreasing open circuit voltage.[45,46] During the downward part of temperature cycling, small hysteresis effects are observed, but no major signs of temperature-induced irreversibility are found, the module thus returning to its initial performance at 25 °C.

2.2. Outdoor monitoring

For outdoor monitoring, a set of two OPV modules of module batch_A (see Section 4 for details) and two m-Si modules (Hörmann Novo Solar GmbH) were selected. The geometric fill

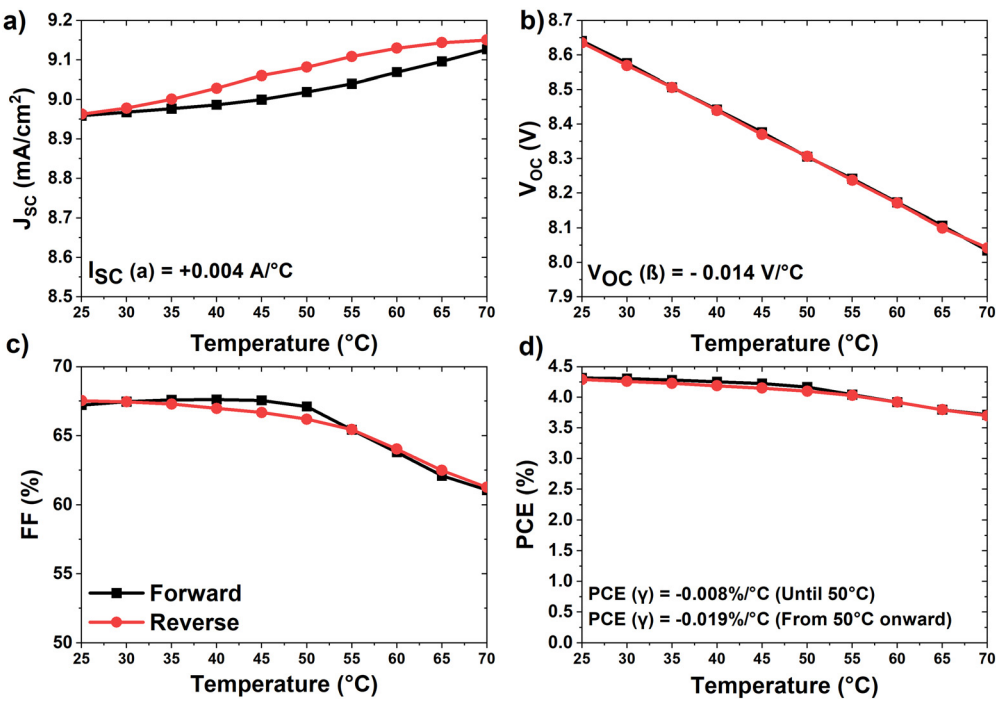

Fig. 2 Effect of temperature on the key photoelectrical parameters (a) temperature dependence of J_{SC}, (b) temperature dependence of V_{OC}, (c) temperature dependence of FF, and (d) temperature dependence of PCE) of the OPV module over a temperature range of 25–70 °C under AM1.5G conditions during upward (black) and downward (red) direction.

Table 1 STC t_0 performance of modules and their respective orientations for outdoor monitoring experiments. The temperature coefficient of the PCE is valid over the temperature range of 25–50 °C

Module type	Outdoor inclination	Area (m^2)	P_{OUT}(STC) (W)	V_{OC} (V)	I_{SC} (A)	FF (%)	Module efficiency (%)	Temperature coefficient of PCE (γ, % $°C^{-1}$)
m-Si #1	45°	0.25	30.35	10.05	3.97	75.9	12.11	−0.35
m-Si #2	90°	0.25	30.72	10.19	3.95	76.3	12.28	−0.35
OPV #1	45°	0.021	0.98	14.4	0.10	68.2	4.68	−0.008
OPV #2	90°	0.021	0.99	14.4	0.10	68.5	4.70	−0.008

factor (GFF) of the reference m-Si modules was around 64%. The modules were first measured at t_0 under STC using a flasher light source. The OPV modules were light-soaked at 1000 W m^{-2} for 30 min before the measurement to achieve maximum performance. The t_0 values of the modules are listed in Table 1.

The location for outdoor monitoring was Erlangen, Germany, with site coordinates of 49.5897°N and 11.0120°E. The OPV and m-Si modules were mounted at a tilt angle of 45° with respect to the horizontal (corresponding to the optimal tilt angle of the site, which is mostly observed for rooftop installations) and at a vertical inclination of 90° with respect to the horizontal (corresponding to the module orientation within a BIPV façade). m-Si #1 and OPV #1 were mounted at an inclination of 45°, whereas m-Si #2 and OPV #2 were mounted at a 90° inclination (Table 1) and are referred to as m-Si 45°, OPV 45°, m-Si 90°, and OPV 90° from this point onwards. All modules faced south to maximize the yearly energy harvest. For outdoor measurements, an open-rack test configuration was used to avoid excessive module heating (Fig. S8, ESI†). All modules were measured under maximum power point (MPP) conditions using an automated MPP tracking system (Automatic Research GmbH). The MPP tracker determines the MPP by adjusting a variable electronic resistor and returns the power output (P_{OUT}), maximum power point current (I_{MPP}), maximum power point voltage (V_{MPP}), V_{OC}, and I_{SC} for each MPP condition. The temporal resolution of the MPP tracker is three minutes between two consecutive measurements. Between the measurements, the modules were kept under open-circuit conditions. For each MPP measurement, the module temperatures (T_{MOD}) and the in-plane irradiance were measured (embedded with the system clock). The PT100 temperature sensors were glued to the backside of each module using a thermal adhesive to monitor the T_{MOD}. Additionally, the ambient air temperature (T_{AMB}) was recorded using the PT100 temperature sensors. A set of irradiance sensors (Fronius, calibrated at 70 mV for 1000 W m^{-2}, ±5% annual tolerance) were used to record the daily in-plane irradiance values at both inclinations of 45° and 90°. The measurement data was stored as a daily data file on a local server, accessible *via* LAN for post-data processing. These data are later used to determine the annual energy yield and outdoor performance of both module types (Section 2.3).

In the first week of outdoor monitoring, the diurnal performances of the OPV and m-Si modules were compared on two different days with contrasting weather conditions. For this purpose, a sunny day with a relatively large contribution from direct irradiance (28.06.2019) and an overcast day with a large contribution from diffuse irradiation (07.07.2019) were selected for comparative analysis (Fig. S9, ESI†). To investigate the effect of the operational conditions on the performances of both module types of different nameplate efficiencies, the normalized power output (P_{Norm}) is calculated from the actual power output $P_{OUT}(t)$ of the module and its power output under STC, P_{OUT}(STC), as defined by eqn (1).

$$P_{Norm}(t) = \frac{P_{OUT}(t)}{P_{OUT}(STC)} \quad (1)$$

To measure the average performance of both module types over extended periods of time (a day or a year), we employ the specific energy yield, $Y_{F,tmax}$ as a performance metric for comparative outdoor analysis. $Y_{F,tmax}$ refers to the amount of energy (W h) produced for every W_P of module capacity over the course of a certain time or complete year. It is obtained by integrating the numerator of eqn (1) over the respective period, according to eqn (2) and is measured in the units (W h W_P^{-1}).

$$Y_{F,t_{max}}\left(\text{W h W}_P^{-1}\right) = \frac{\int_{t=0}^{t_{max}} P_{OUT}(t)\mathrm{d}t}{P_{OUT}(STC)} \quad (2)$$

For t_{max} = 24 hours, the daily specific energy yield, Y_{FD}, is obtained, with the daily energy harvest E_D being defined by eqn (3).

$$E_D\ (\text{W h}) = \int_{t=0}^{24\ \text{h}} P_{OUT}(t)\mathrm{d}t \quad (3)$$

The diurnal development of Y_{FD} for both module types at their respective inclinations is shown in Fig. 3 for both days, along with the measured values of in-plane irradiance, angle of incidence of the sun with respect to the surface normal of the modules at their respective mounting angles, and the module temperature (T_{MOD}).

On the clear sunny day of 28.06.2019, maximum solar irradiances of close to 950 W m^{-2} and 520 W m^{-2} were observed, at inclinations of 45° and 90°, respectively (Fig. 3(a)). The T_{MOD} patterns of both module types followed the in-plane irradiance and reached a maximum at solar noon, *i.e.*, around 13:00 hours CEST (Fig. 3(b)). At 45° inclination, the maximum T_{MOD} of m-Si reached close to 55 °C, whereas for OPV it is approximately 47 °C, *i.e.*, the OPV module operated at T_{MOD} which was on average 5–8 °C lower than that of the m-Si module. For 90° inclinations, the T_{MOD} difference between the two module types was marginal. The maximum T_{MOD} at this inclination is close to 43 °C for the m-Si module, whereas for the OPV, it reaches 39 °C. The minimum sun angle with

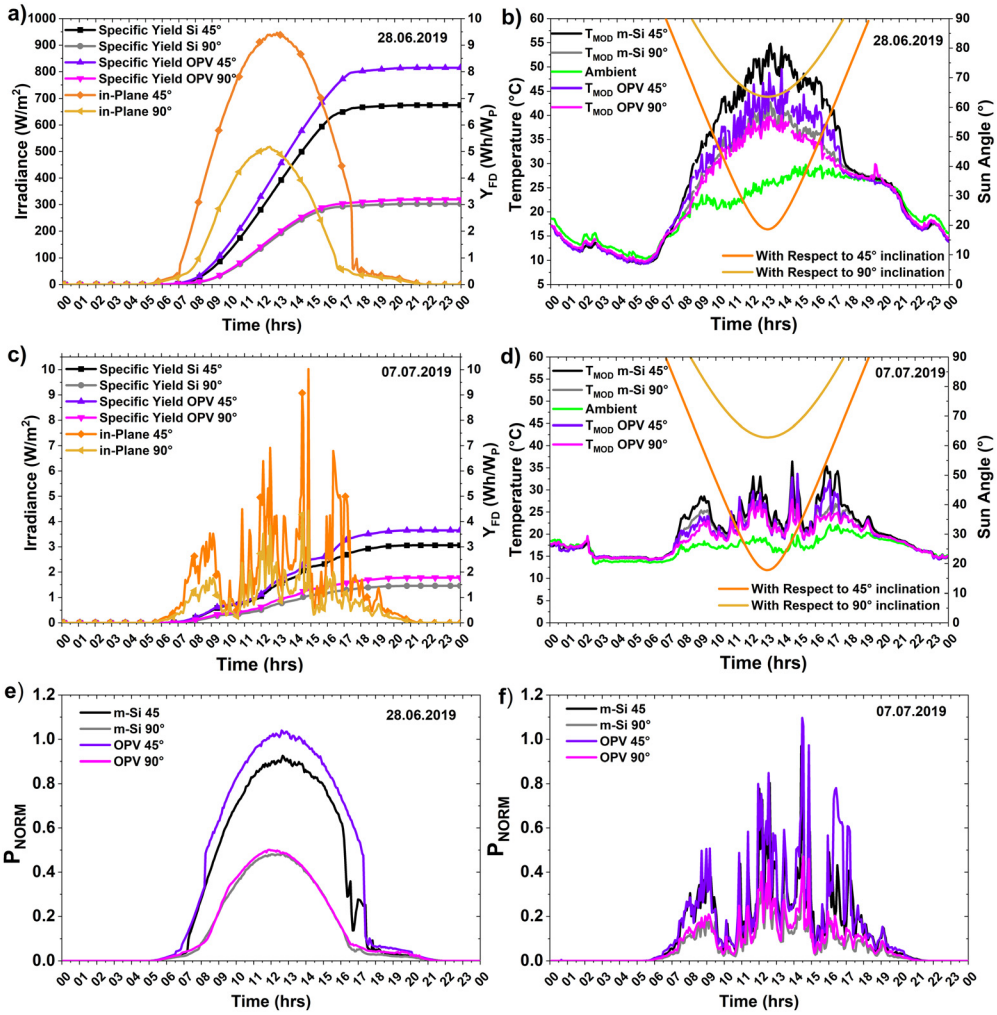

Fig. 3 Diurnal time-traces (hours indicate Central European Summer Time) of (a) integrated daily specific energy yields (Y_{FD}) of OPV and m-Si modules along with the measured in-plane irradiance at 45° and 90° inclinations on a clear sunny day (28.06.2019), (b) module operating temperatures, ambient temperatures, and sun angles with respect to the surface normal of the modules for a sunny day (28.06.2019), (c) Y_{FD} of OPV and m-Si modules along with the measured in-plane irradiance at 45° and 90° inclinations on an overcast day (07.07.2019), (d) module operating temperatures, ambient temperatures and sun angles with respect to the surface normal of the modules over an overcast day (07.07.2019), (e) time-resolved traces of P_{Norm} on the clear sunny day (28.06.2019) and (f) time-resolved traces of P_{Norm} on an overcast day (07.07.2019).

respect to the surface normal of the modules was observed at solar noon (13:00 hours CEST), which is approximately 19° for 45° inclination, and approximately 65° for 90° inclination (Fig. 3(b)). At 45° inclination, the average Y_{FD} of the OPV module was approximately 21% higher than that of the m-Si module, whereas at 90° inclination, the Y_{FD} of the OPV module exceeded that of the m-Si module by only 6% (Fig. 3(a)). Between 9:00 CEST-17:00 hours CEST more than 85% of the total electrical energy harvest for the day is generated (Fig. 3(a)). During this period, the T_{MOD} of both module types significantly exceed the STC temperature of 25 °C (Fig. 3(b)). While the temperature-induced PCE losses over the observed T_{MOD} range are negligible for the OPV modules at both inclinations, up to a maximum of 10% and 6% performance losses are observed around noon for the m-Si module at 45° and 90° inclination, respectively (Fig. 3(e)). The effect of the angle of incidence on module performance is only significant for the vertical modules, except for the early morning and late evening hours. The higher Y_{FD} value of the OPV module at 45° inclination as compared to the corresponding m-Si module can thus be ascribed to its lower temperature coefficient γ. In contrast, for the vertical modules, the angle of incidence is larger than 60° over the whole day, which leads to significant reflection losses for both module types (Fig. 1 and Fig. S10, ESI†). These losses are larger for the OPV module than for the m-Si modules (Fig. 3(e)), which practically compensates the temperature-induced performance advantages, resulting in almost equal Y_{FD} values for OPV and m-Si modules (Fig. 3(a)). It should also be noted that the performance of the OPV modules slightly improves during the early few days of outdoor exposure, especially in the months of high irradiance due to the light soaking effect (Fig. 3(e)).

On the overcast day of 07.07.2019 (Fig. 3(c)), the temporal solar irradiance pattern was dominated by clouds and

contained mainly contributions from diffuse irradiance (Fig. S9, ESI†).[47] Under these weather conditions, the average Y_{FD} for both module types are observed to be approximately 45% and 55% of their respective values on sunny days, for inclinations of 45° and 90°, respectively (Fig. 3(c)). For both module inclinations, the average Y_{FD} over the whole day for the OPV modules was approximately 20% higher than that of the m-Si module (Fig. 3(a)). Like on sunny days, the main energy harvesting period of the day lies between 9:00 and 17:00 hours CEST. During this period, the difference in T_{MOD} between the two module types was marginal for both inclinations (Fig. 3(d)), thus providing the OPV modules with a slight performance advantage over the m-Si modules, as evident from the respective values of Y_{FD} in Fig. 3(f). However, the main advantage of the OPV modules under the overcast weather conditions arises from their good low light performance (Fig. 3(f)). For the modules at 45° inclination, the angle of incidence hardly affects the performance of both module types between 9:00 and 17:00 hours CEST, as indicated by the respective curves in Fig. 1. This is also true for the vertical modules, as they receive mainly diffuse irradiation. In summary, the superior performance of OPV modules on days with overcast conditions mainly stems from their good low-light performance, in combination with good performance under diffuse light conditions.

The daily energy yields of both module types at their respective outdoor inclinations on both clear and overcast days are summarized in Table 2. The table also provides the performance ratio (PR) of both module types at their respective inclination. PR describes the performance of the modules under the actual operational conditions with respect to a hypothetical daily reference yield (Y_{RD}) as defined by eqn (4). Y_{RD} is described by eqn (5) as the ratio of daily global in-plane irradiance (kW h m^{-2}) and G_0 = 1000 W m^{-2}.

$$\mathrm{PR} = \frac{Y_{FD}}{Y_{RD}} \tag{4}$$

$$Y_{RD} = \frac{\text{in-plane irradiance } (\mathrm{kW\ h\ m^{-2}})}{G_0} \tag{5}$$

As indicated by the PR, the OPV modules show operational performances which are superior to their STC performances, especially under very high and very low irradiation conditions, due to their small temperature coefficient and better low light behavior, respectively.

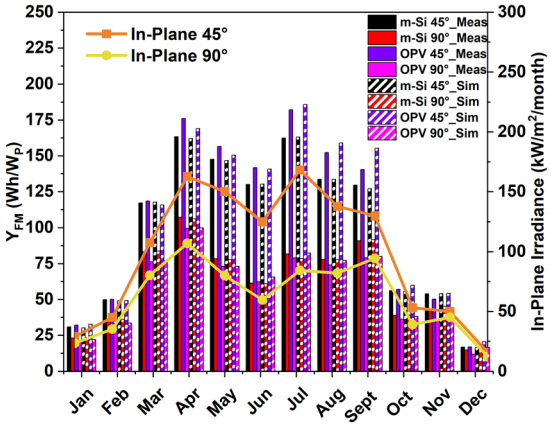

Fig. 4 Recorded monthly-specific-energy-yields (Y_{FM}) of both OPV and m-Si modules over the year at 45° (m-Si #1 and OPV #1) and 90° (m-Si #2 and OPV #2) angles of inclination (solid columns). The respective simulated Y_{FM} of both module types at their respective outdoor inclinations over the year is represented by dashed columns of the same color. The recorded monthly in-plane irradiance over the year is represented by orange lines for 45° and yellow lines for 90°.

2.3. Long-term outdoor monitoring

The outdoor performance of both module types was monitored over a year, following the methods described in Section 2.2 with a monitoring period spanning from 01.01.2020 to 31.12.2020. The measured monthly-specific-yield Y_{FM} (Exp) is calculated by eqn (2) with t_{max} = 1 month from the experimental data and was utilized as a performance metric for comparative analysis of both module types at their respective inclinations. The Y_{FM} (Exp) values recorded over the course of the outdoor monitoring period are plotted in Fig. 4 and summarized in Table S3, ESI.†

The performance differences between the OPV and m-Si modules can be quantitatively understood by comparing their experimental Y_{FM} (Exp) traces to simulated ones, Y_{FM} (Sim), which use the respective laboratory angle (θ), in-plane light intensity (I), and temperature-dependent (γ) PCE responses of both module types as determined from the lab experiments in Section 2.1, to calculate the Y_{FM} (Sim) traces from the T_{MOD}, angles of incidence, and irradiation conditions observed during the outdoor monitoring, according to eqn (6).

$$Y_{FM}(\mathrm{Sim}) = \frac{\int_{t=0}^{1\ \mathrm{month}} P_{OUT(Sim)}(I,\theta,\gamma)\cdot \mathrm{d}t}{\mathrm{STCW_P}} \tag{6}$$

Table 2 Diurnal performance of OPV and m-Si modules on sunny (28.06.2019) and overcast (07.07.2019) days at their respective inclination angles

Date	Module & orientation	Total daily energy harvest E_d (W h day^{-1})	Global in-plane irradiance (kW h m^{-2} day^{-1})	Y_{FD} (W h W$_P^{-1}$)	PR
28.06.2019	m-Si 45°	205	7.01	6.75	0.96
28.06.2019	m-Si 90°	93	3.21	3.02	0.94
28.06.2019	OPV 45°	8.15	7.01	8.15	1.16
28.06.2019	OPV 90°	3.2	3.21	3.2	1
07.07.2019	m-Si 45°	92.84	3.08	3.06	0.99
07.07.2019	m-Si 90°	44.65	1.49	1.45	0.97
07.07.2019	OPV 45°	3.65	3.08	3.65	1.19
07.07.2019	OPV 90°	1.78	1.49	1.78	1.20

In eqn (6), the $P_{OUT(Sim)}$ is obtained using the following eqn (7):

$$P_{OUT(Sim)}(I,\theta,\gamma) = \beta(I)\cdot\mu(\theta)\cdot\gamma(T)\cdot\text{module area}\cdot I \quad (7)$$

where γ, β, and μ are obtained from the PCE curves in Fig. 1 and 2(d) according to eqn (8)–(10). For the m-Si modules, $\gamma(T)$ is calculated from the temperature coefficients in Table 1.

$$\gamma(T) = \frac{\text{PCE}(T)}{\text{PCE (25 °C)}} \quad (8)$$

$$\beta(I) = \frac{\text{PCE}(I)}{\text{PCE (AM1.5)}} \quad (9)$$

$$\mu(\theta) = \frac{\text{PCE}(\theta)}{\text{PCE}(I@\theta)} \quad (10)$$

The resulting Y_{FM} (Sim) values are plotted in Fig. 4, next to their experimental counterparts, Y_{FM} (Exp), and are also summarized in Table S3 (ESI†). At first instance, the Y_{FM} values of both module types follow the monthly incident in-plane irradiance at their respective inclinations. The monthly in-plane irradiance is impacted by the annual changes in solar elevation angles observed with respect to the modules (Fig. S11, ESI†). High monthly in-plane irradiances occurred between April and September. During these months, the incident in-plane irradiance at 90° inclination is almost half of that observed at 45°. Conversely, the differences between the in-plane irradiances at both inclinations begin to diminish during late autumn to late winter (October to January), with the modules at 45° inclination receiving slightly more irradiation than their 90° inclination counterparts. T_{MOD} is also impacted by seasonal variations, with the highest average T_{MOD} being reported during the summer months (May to August) for both module types (Fig. S12, ESI†). In the months when the modules mostly operate under clear sunny conditions and higher T_{MOD} are observed, *i.e.*, from April to September, the OPV module at 45° inclination shows higher Y_{FM} (Exp) values than the corresponding m-Si module. As demonstrated in Section 2.2, the impact of T_{MOD} on the Y_{FM} (Exp) of the OPV modules at both inclinations is minimal due to their negligible temperature coefficient as they operate at $T_{MOD} < 50$ °C year-round (Fig. S12, ESI†). Conversely, the influence of T_{MOD} on the Y_{FM} (Exp) is notable for m-Si modules, due to their relatively large negative temperature coefficient. In July, when T_{MOD} reaches 58 °C, the temperature-induced PCE losses of the m-Si modules at 45° inclination amount to up to 11%. At 90° inclination, the impact of T_{MOD} on PCE still leads to a loss of up to 9% for the maximum T_{MOD} of around 53 °C observed in August (Fig. S12, ESI†). Nevertheless, at 90° inclination, both module types yield almost identical Y_{FM} (Exp) values during these months. The reason is that the Y_{FM} (Exp) values of both module types are also greatly affected by the yearly changes in solar elevation angles. For modules at 45° inclinations, the angle of incidence of direct irradiance at noon varies approximately between 0° and 30° throughout the year, while for 90° inclinations, this variation is between 20° and 60° (Fig. S11, ESI†). Therefore, the Y_{FM} (Exp) values of both module types inclined at 90° are greatly affected by their angle-dependent response as determined during the laboratory investigations, with m-Si module clearly having an advantage over the OPV modules for the months of high irradiance, according to Fig. 1 (*i.e.*, April to September). Thus, for these months, the temperature-induced performance losses of the m-Si module are slightly overcompensated by the higher losses of the OPV modules at high angles of incidence.

While the simulations conveniently explain the course of the Y_{FM} values over the year for both module types, it is worth having a more quantitative look at the predictions of the model. The relative deviations between the experimental and simulated Y_{FM} values vary between −0.5% and 2.4% for m-Si 45°, whereas for m-Si 90°, such deviations range between −3.7% and 4%. For OPV modules, the relative deviations between the experimental and simulated Y_{FM} values vary between −9.5% and +4.2% at 45° inclination, with an outlier of −18.3% in December. At 90° inclination, such deviations range between −0.1% and −5.2%, with outliers of −15.5% and −28.1%, in November and December, respectively. For the average annual specific energy yields (Y_{FA}), the deviations are around ±1% and ±5% on average for m-Si and OPV modules, respectively, when neglecting the outliers (Table S3, ESI†). For the m-Si modules, the simulations are thus in reasonable accordance with the experimental values throughout the monitoring period, which indicates that the model comprises the most important effects of operational conditions on device performance. The somewhat larger deviations between simulated and experimental data for OPV will be addressed below, based on the presentation in Fig. 4.

For the OPV modules at both inclinations, the relative deviation between recorded and simulated Y_{FM} values was ≤±5% throughout the period of January to October, except for September, when the Y_{FM} (Exp) value of the OPV module at 45° inclination was less than the corresponding Y_{FM} (Sim) value by around 9%. From March to June, the experimental values of Y_{FM} for the OPV module at 45° increased continuously with respect to the simulated ones. One of the major reasons for this performance improvement is enhanced light soaking of the ETL by the increasing irradiance (Fig. S6, ESI†). From June onwards, this trend is reversed for both module inclinations. For OPV 45° module this results in experimental Y_{FM} values which are smaller than the simulated ones from July onwards. Finally, in November and December, the experimental Y_{FM} values are substantially smaller than the simulated ones for both inclinations (Table S3, ESI†). We ascribe this increasing deviation to the degradation of the modules, which is continuous until October and subsequently results in catastrophic failure.

To validate this claim, the PCE degradation traces of OPV modules are plotted as a function of the energy dose of light received by the modules throughout outdoor exposure (Fig. 5), together with the corresponding data gathered during the ALT under ISOS-L2 conditions (data taken from Fig. 6(d)). The outdoor data are collected following the ISOS-O2 recommendations, *i.e.*, data points were collected only for irradiance

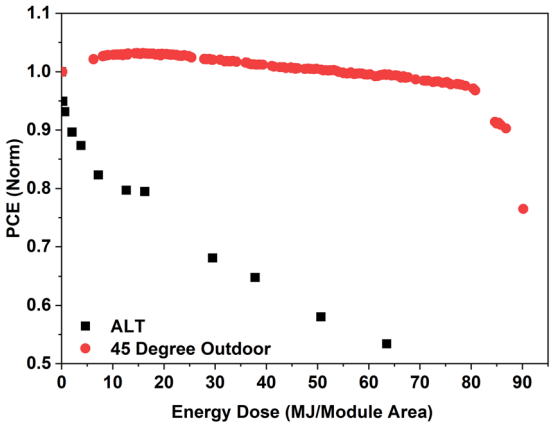

Fig. 5 PCE values, normalized to t_0 performance, as a function of light energy dose incident onto the module surface in megajoules (MJ) during accelerated lifetime testing (black points) and during the one-year outdoor exposure at a 45° inclination angle (red points).

values greater than 800 W m^{-2}. As the vertical modules hardly received any irradiance greater than 800 W m^{-2}, we confine our analysis to the outdoor PCE values obtained for the OPV 45° module. Initially, the PCE improves with increasing light dose, due to the light soaking effect. It is worth noting that this effect is responsible for the recorded Y_{FM} values growing with respect to the simulated ones in the months of March to June as described above. Starting at a dose of around 15 MJ, the PCE decreases slowly but steadily. At a dose of 80 MJ, *i.e.*, at the end of September, the module still provides more than 95% of its initial performance. Subsequently, the device performance drops sharply by around 20% with the t_{80} lifetime of the module being reached at a light dose of around 90 MJ. Visual inspection of the OPV modules does not show any signs of encapsulation failure/delamination or ingress of humidity and oxygen through the contact points, as it had been observed during a previous outdoor test (Fig. S13, ESI†). The comparison of the *IV*-curves recorded with a flasher light source before and after degradation (Fig. S14, ESI†) reveals that the catastrophic failure of the OPV modules after one year arises from the combination of V_{OC} and FF losses (for the corresponding key performance indicators, see Table 3). This observation is in accordance with the dark lock in thermography (DLIT) images of the OPV modules recorded before and after the outdoor exposure which point to the development of a large number of localized shunts during outdoor operation, as shown in Fig. S15, (ESI†).[48]

2.3.1. Accelerated lifetime (ALT) testing. To understand the ageing behavior of the OPV modules during the outdoor

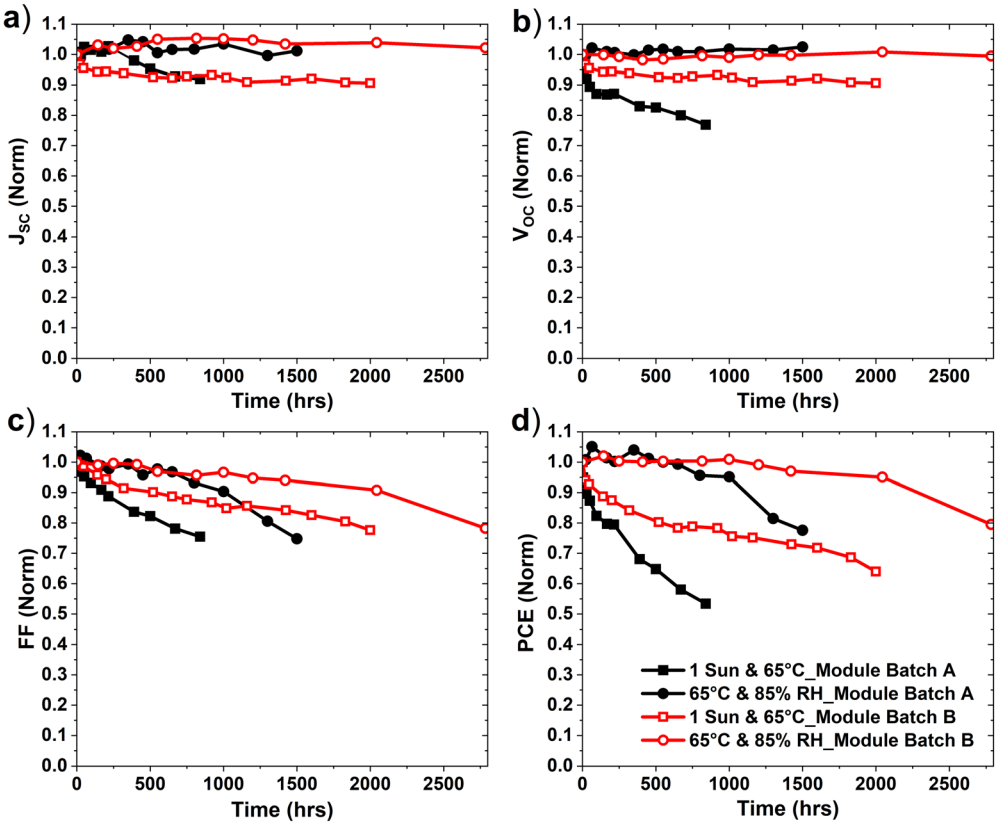

Fig. 6 Time traces of the PV key performance indicators during accelerated lifetime testing (ALT) of module batch_A (solid symbols) and module batch_B (open symbols), normalized to their respective t_0 values. Circles indicate the time traces for ISOS-D3 conditions (65 °C module temperature and 85%RH), while squares indicate ISOS-L2 conditions (1000 W m^{-2} light intensity and 65 °C module temperature). (a) Short-circuit current density (J_{SC}), (b) open-circuit voltage (V_{OC}), (c) fill factor (FF), and (d) power conversion efficiency (PCE).

Table 3 Key performance parameters of the OPV modules after one year of outdoor exposure, measured at STC

Modules	P_{OUT} (W_P)	V_{OC} (V)	I_{SC} (A)	V_{MPP} (V)	I_{MPP} (A)	FF (%)	Efficiency (%)	Rel. difference with respect to efficiency @ t_0 (%)
OPV #1	0.77	12.5	0.11	8.62	0.09	58.2	3.64	−23
OPV #2	0.74	12.5	0.102	8.60	0.09	57.5	3.50	−26

monitoring period, ALT studies on OPV modules were performed. The modules were subjected to ALT testing under ISOS-L2 and ISOS-D3 conditions, the results of which are shown in Fig. 6. The temporal evolution of the current–voltage (*I–V*) characteristics during ALT testing of both module batches is shown in Fig. S16, ESI.† For ISOS-L2 conditions, SUNTEST XLS+ (Atlas materials testing solutions) equipped with xenon arc lamp and daylight filter (Fig. S17, ESI†) was used as both the light and heat source for the ALT investigations. The ALT test was discontinued once the t_{80} lifetime benchmark (the time when the module has lost 20% of its initial performance) had been reached for the respective testing conditions. Two different module batches were investigated: module batch_A, with a D : A ratio of 1 : 1 and module batch_B with a D : A ratio of 1 : 1.5 (see Section 4 for details). Module batch_B was manufactured after the end of the outdoor monitoring period of module batch_A, to explore possible ways of enhancing module lifetime.

As shown in Fig. 6(d), module batch_A exhibits a t_{80} lifetime of approximately 1500 h under ISOS-D3 conditions. The modules show good stability in terms of their short-circuit current density (J_{SC}) and open-circuit voltage (V_{OC}), whereas a constant fill factor (FF) drop due to increasing series resistance is observed from the beginning, which accelerates after around 750 h. Under ISOS-L2 conditions, J_{SC} also remains constant first, but shows a linear drop from around 250 h onwards (Fig. 6(a)). For the V_{OC}, a burn-in period is observed which saturates after around 100 h, followed by a linear decrease starting at around 250 h (Fig. 6(b)). The FF undergoes a constant drop from the beginning, similar to ISOS-D3 conditions, but more pronounced (Fig. 6(c)). The FF loss is due to increasing series resistance, which at later stages even turns into an S-shaped *IV*-curve. Overall, the combination of FF and V_{OC} losses accounts for the majority of PCE losses for module batch_A under ISOS-L2 conditions, resulting in a lifetime of 215 h. In conclusion, in the dark, the packaged modules are stable against heat, oxygen and humidity for around 1200 hours, whereas their lifetime is critically reduced upon concomitant exposure to heat and light.

The fact that the FF losses observed for module batch_A under illumination are caused by increasing series resistance (Fig. S16, ESI†), is a strong indication for the deterioration of one or both of the interfaces between PAL and the charge extraction layers.[49] Also the concomitant V_{OC} losses are in accordance with interface issues, such as the oxidation by oxygen released by the ETL or the deterioration of the PAL/HTL interface.[14,50] In previous experiments, it had been found that by only increasing the HTL thickness from 20 nm to 100 nm the lifetimes of the modules of batch_A are enhanced significantly (Fig. S18, ESI†), by stabilizing V_{OC} and J_{SC} as well as by reducing FF losses.

To test the hypothesis of the relatively thin HTL of only 100 nm of module batch_A being the cause for the encountered stability issues, a modified module batch_B was produced, in which the HTL thickness was further increased to 150 nm. Concomitantly, the PAL ink recipe was changed by increasing the donor : acceptor ratio from 1 : 1 for batch A to 1 : 1.5 in batch B and by varying the solvent composition (for details see Section 4). Compared to module batch_A, the resulting module batch_B shows a significantly enhanced t_{80} lifetime of more than 2800 h under ISOS-D3 conditions (Fig. 6), due to the less pronounced FF losses (Fig. 6(c)). Under ISOS-L2 conditions, the modules of batch_B exhibit a t_{80} lifetime of close to 1000 h (Fig. 6(d)), which is improved with respect to module batch_A by a factor of around four. On the one hand, this is due to reduced burn-in losses of J_{SC} and especially of V_{OC}, both of which stabilize after the initial 20 h. On the other hand, module batch_B shows a FF drop, which is significantly less pronounced than that of module batch_A, but nevertheless is continuous and eventually leads to device failure. The reduced V_{OC} and FF losses in module batch_B with its increased HTL thickness supports the above hypothesis that strengthening the PAL/HTL interface makes the modules less sensitive to degradation by simultaneous exposure to light and heat. However, it also becomes clear from the comparison of Fig. 6 and Fig. S19, ESI† that the lifetime of module batch B has benefitted significantly from improving the morphology of the PAL layer by changing the D : A ratio to 1 : 1.5, while employing of different solvent mixtures for the preparation of batch_A shows no effect on the lifetimes of the modules (Fig. S19 and S20, ESI†).

2.3.2. Correlation between ALT and OLT. When comparing performance degradation of OPV module batch_A observed in ALT and OLT tests, the most striking difference is the much faster degradation under ISOS-L2 conditions in terms of incident light dose. As shown in Fig. 5, the OPV module tested under ISOS-L2 conditions degraded continuously and rapidly, reaching its t_{80} lifetime at a light dose of approximately 16.25 MJ, *i.e.*, at 215 h. As one would expect from the ALT tests in Section 2.3.1., where the combination of light and heat was identified as the main factor for device degradation, ALT and OLT degradation should follow the irradiated light dose in a very similar way. However, while the module has lost 20% of its initial performance at around 16 MJ in the ALT investigations, it shows not more than 5% performance loss at 80 MJ under outdoor conditions. Possible reasons that may contribute to this discrepancy are nonlinear response to light intensity[51] (the intensities under outdoor conditions are always less than 1 sun), different light spectra (the light spectrum in ALT testing is modified by a day light filter, but has relatively high intensity between 450 and 550 nm, to which the PAL is overly sensitive, as demonstrated by Hintz and Heumüller,[52,53] the significantly lower temperatures under outdoor conditions (T_{MOD} of the OPV modules hardly ever exceeds 50 °C at either inclination during

their actual outdoor operation and most of the time stays at an average T_{MOD} close to STC during the months), or recovery effects.[54] An example of a recovery effect revealed during our studies concerns ALT tests under damp heat conditions. Modules kept in dark and damp-heat conditions for extended periods (weeks) show performance drops due to the lack of light soaking, which can be easily recovered through light exposure. Consequently, modules under outdoor conditions do not suffer from this effect, at least not to this extent, as they are light-soaked regularly during daytime. Other recovery mechanisms, such as recovery overnight,[54] have not been studied systematically in our labs but have been reported in literature for devices similar to ours. Previously, our group reported P3HT:o-IDTBR based devices incorporating evaporated silver top electrode to be stable for 2000 h (<10% degradation) upon illumination under the LED light source (1000 W m^2 with no UV content) and by avoiding device heating.[35] Also the devices based on P3HT:o-IDTBR show enhanced oxidative stability (<20% degradation) for unencapsulated devices kept under dark ambient conditions.[36] These literature reports further support our findings that the faster degradation during ALT is primarily due to the simultaneous exposure to heat, light, and increased UV content. Further OLT studies will be necessary to elucidate the reasons for the observed difference in degradation rates.

Similarities and differences between ALT and OLT are found when analyzing the changes of the *IV*-curve of the OPV45° module in January 2021, *i.e.*, after its catastrophic failure (Fig. S14, ESI†). In both cases, the I_{SC} is hardly affected, while V_{OC} and FF losses lead to device failure. However, more detailed analysis reveals differences in the reasons for the FF losses. In ALT, the FF is reduced due to the increasing series resistance exclusively, which hints at an issue at the PAL/HTL interface, as confirmed by the reduced degradation rate upon increasing the HTL thickness. In OLT, however, the series resistance hardly changes, instead shunts appear in the DLIT images (Fig. S15, ESI†), along with an increasing slope of the *IV*-curve in the 4th quadrant (Fig. S14, ESI†). These differences in device degradation behavior taken together lead to the conclusion that the degradation mechanisms under the conditions of ALT and OLT are not directly comparable. Thus, while it may seem tempting to deduce an ALT *vs.* OLT acceleration factor of around five from Fig. 5, the lack of understanding of the underlying degradation mechanism under the respective conditions makes it difficult to express their relative rates by a simple acceleration factor. Further ALT/OLT studies will be necessary to understand the factors which are responsible for the degradation of the OPV modules under outdoor operational conditions.

3. Conclusion

In conclusion, we present the long-term outdoor characterization of fully R2R printed solution-processed flexible large-area OPV modules. Comparative outdoor studies were conducted over the course of a year in typical central European climatic conditions, within the context of BIPV installation. Two different mounting conditions, namely south faced 45° and 90° inclinations, were investigated, as they represent the most relevant scenarios for BIPV applications. The results demonstrate that, on days with high levels of in-plane irradiance, the OPV modules at 45° exhibited approximately 21% higher Y_{FD} than the m-Si modules at the same inclination. This difference can be attributed to the better temperature coefficient of the OPV modules. For 90° inclination, the Y_{FD} difference between the two module types was approximately 6% in favor of OPV, resulting from a partial compensation between the negligible temperature coefficient of the OPV module and the relatively better angle-dependent response of the m-Si module, achieved by the anti-reflection coating of the latter. Under overcast conditions, the OPV modules outperformed the m-Si modules with a Y_{FD} advantage of 20% and 22% at 45° and 90° inclinations, respectively, mainly due to their good performance under low and diffuse light conditions.

These characteristics of the different module technologies were also reflected in their behavior observed throughout the year-long monitoring period, as the performance of both module types was influenced by seasonal variations in the T_{MOD} and the angle of incidence with respect to the sun. During summer months, when high levels of in-plane irradiance were present, the OPV modules showed higher Y_{FM} compared to the m-Si modules at 45° inclination. At 90° inclination, the angle-dependent response of both module types played a significant role, resulting in identical Y_{FM} values during periods of high in-plane solar irradiance *i.e.* summers. Furthermore, the study demonstrated that quantitative modeling based on the collected data enables accurate prediction of energy harvest of OPV modules using transient weather data. By considering the indoor angle, light, and temperature-dependent response of both module types, the energy harvest prediction achieved a precision of 5% or better. Increasing deviations between measured and predicted performances during the outdoor monitoring period have been demonstrated to serve as a reliable indicator for module degradation.

With the help of systematic modifications of HTL thickness and donor.acceptor ratio in the photoactive layer, the module lifetime was enhanced, as monitored in ALT according to ISOS-L2 and ISOS-D3 standards. The findings of this study significantly enhance our understanding of the potential and practical applications of OPV, particularly in the context of BIPV installations. By incorporating certain optical management techniques to mitigate the optical losses associated with the OPV module and air interface could thus enable the future OPV modules to offer even better performance for installations where the modules are exposed to the incident sunlight at higher angles of incidence with respect to the sun.

4. Module fabrication

OPV modules of module batch_A were fabricated in an inverted device architecture by using a combination of full-area slot die coating and roll-to-roll (R2R) laser patterning. Flexible PET/IMI

sheets from OPVIUS GmbH were used as substrates. The IMI substrate was laser structured (P1) using a femtosecond laser (Laser Systems GmbH) with a laser fluence of 0.40 J cm^{-2} at a pulse duration of 350 fs and 520 nm wavelength. This leads to the electrical isolation of the IMI bottom electrode into the number of individual cells within the OPV module. All the functional layers of the OPV modules were coated in ambient air, at a coating speed of 0.5 m min^{-1}. The thicknesses of the functional layers were controlled by adjusting the ink flow rates and concentrations. First, a 10 nm thick ETL was coated on top of P1 structured IMI substrates and annealed afterwards at 120 °C for four minutes. The corresponding ink was N31 tin oxide (SnO_2) nanoparticle formulation from Avantama which was filtered with a 0.22 μm PP filter and ultra-sonicated afterwards for 10 minutes before coating. The PAL layer was coated on top of the ETL and dried inline at 85 °C for 1 minute using hot air ovens. The thickness of the PAL was around 250 nm. The photoactive layer (PAL) incorporated a P3HT donor polymer purchased from BASF and a non-fullerene acceptor o-IDTBR purchased from Nano-C. For module batch_A, the PAL ink was prepared in a 1 : 1 donor : acceptor ratio in *o*-xylene and 1-methyl naphthalene (95 : 5) with a total concentration of 30 mg ml^{-1}. The PAL ink was stirred overnight inside the glove box at 80 °C. Highly conductive water-based PEDOT:PSS (HTL-388) purchased from Heraeus GmbH was used as a hole transport layer (HTL) and diluted 1 : 1 with water. Subsequently, 1% silquest and 2% capstone surfactant was added to the total volume to enhance the wetting properties of the HTL. For module batch_A, a thin HTL was coated on top of the PAL and annealed at 140 °C for 4 minutes, thus resulting in a 100 nm thick HTL. Subsequently, the P2 line was laser ablated, which serves as a prerequisite for the electrical interconnection of every adjacent cell within the module. Finally, water-based silver nanowires (AgNW's) purchased from Cambrios were coated. The AgNW's were slot die coated at a speed of 1 m min^{-1}, resulting in a sheet resistance of approx. 8 Ohm sq^{-1}, and subsequently annealed for 2 min at 130 °C. All the annealing processes were carried out inline after each respective coating step. Finally, a P3 laser line was drawn to isolate the AgNW's. The resulting OPV modules of batch_A consist of 20 cells with a total area of 210 cm^2 (including bus bars and cells interconnection area), whereas the active area of the module was 195 cm^2. This resulted in a 93% geometric fill factor (GFF) of the module.

For module batch_B, all the functional layers of the OPV module were processed using doctor blading technique. First, a 10 nm thick tin oxide (SnO_2) ETL was coated on top of P1 structured IMI substrates using a coating speed of 1 mm s^{-1} and annealed afterwards at 120 °C for four minutes in air. The PAL ink for module batch_B was prepared in a 1 : 1.5 donor : acceptor ratio in chlorobenzene and 4-bromoanisole (95 : 5) with a total concentration of 30 mg ml^{-1}. The PAL ink was stirred overnight inside the glove box at 80 °C. The PAL layer was coated on top of the ETL at a coating speed of 35 mm s^{-1} and dried at 140 °C for 4 minutes inside the glovebox. The thickness of the PAL was around 250 nm. Highly conductive water-based PEDOT:PSS (HTL-388) purchased from Heraeus GmbH was used as a hole transport layer (HTL) and diluted 1 : 1 with water. Subsequently, 1% silquest and 2% capstone surfactant was added to the total volume to enhance the wetting properties of the HTL. For module batch_B, a relatively thick HTL was coated on top of the PAL using a coating speed of 10 mm s^{-1} and annealed afterwards at 140 °C for 4 minutes inside the glovebox, thus resulting in a 150 nm thick HTL. Subsequently, the P2 line was laser ablated, which serves as a prerequisite for the electrical interconnection of every adjacent cell within the module. Finally, water-based silver nanowires (AgNW's) purchased from Cambrios were coated on top of HTL twice using a coating speed of 5 mm s^{-1} each (in both forward and reverse directions) resulting in a sheet resistance of approx. 8 Ohm sq^{-1}, and subsequently annealed for 4 min at 120 °C inside glovebox. All the coating steps were performed at a substrate temperature of 65 °C. Finally, a P3 laser line was drawn to isolate the AgNW's. OPV Modules of batch_B consist of 12 cells with a total area of 64 cm^2 whereas the active area of the module was 59.2 cm^2.

All the modules were measured for their initial (t_0) performance using a class AAA solar simulator (LOT Quantum Design). Afterward, the modules were laminated inside a barrier foil from Mitsubishi Chemicals (VD-K3DA) with a UV cutoff filter below 380 nm using UV curable glue (LP655) from DELO GmbH. The entire encapsulation process was carried out under ambient conditions.

Author contributions

S. F. performed the experiments, analysed the data, and wrote the original manuscript. M. W. made the R2R type modules. F. H. designed the outdoor data acquisition equipment. L. D. and I. A. C. were involved in the discussion of the manuscript. H.-J. E. and A. D. supervised the work and the writing of the manuscript. C. J. B. reviewed the manuscript. All the co-authors discussed the results and commented on the manuscript.

Data availability statement

The data that support the findings of this study are available in the ESI.†

Conflicts of interest

The authors declare no conflict of interest.

Acknowledgements

The authors acknowledge funding from the European Union's Horizon 2020 research and innovation program under grant agreement no. 952911 (''BOOSTER'') and from the Federal Ministry for Economic Affairs and Climate Action (BMWK) within ''Fassade^3'' (FKZ 03SBE0008C). Part of this work has been supported by the Helmholtz Association in the framework of the innovation platform ''Solar TAP''. Also, the 'Solar Factory

of the Future' as part of the Energy Campus Nürnberg (EnCN) is acknowledged, which is supported by the Bavarian State Government (FKZ 20.2-3410.5-4-5). H.-J. E. and C. J. B. acknowledge funding from the European Union's Horizon 2020 INFRAIA program under grant agreement no. 101008701 ('EMERGE').

References

1 B. Zimmermann, H.-F. Schleiermacher, M. Niggemann and U. Würfel, *Sol. Energy Mater. Sol. Cells*, 2011, **95**, 1587–1589.
2 F. C. Krebs, *Sol. Energy Mater. Sol. Cells*, 2009, **93**, 394–412.
3 M. Kaltenbrunner, M. S. White, E. D. Głowacki, T. Sekitani, T. Someya, N. S. Sariciftci and S. Bauer, *Nat. Commun.*, 2012, **3**, 770.
4 C. J. Brabec, N. S. Sariciftci and J. C. Hummelen, *Adv. Funct. Mater.*, 2001, **11**, 15–26.
5 B. Azzopardi, C. J. Emmott, A. Urbina, F. C. Krebs, J. Mutale and J. Nelson, *Energy Environ. Sci.*, 2011, **4**, 3741–3753.
6 B. van der Wiel, H.-J. Egelhaaf, H. Issa, M. Roos and N. Henze, *MRS Online Proc. Libr.*, 2014, **1639**, 1003.
7 Z. Zheng, J. Wang, P. Bi, J. Ren, Y. Wang, Y. Yang, X. Liu, S. Zhang and J. Hou, *Joule*, 2022, **6**, 171–184.
8 X. Dong, Y. Jiang, L. Sun, F. Qin, X. Zhou, X. Lu, W. Wang and Y. Zhou, *Adv. Funct. Mater.*, 2022, **32**, 2110209.
9 R. Basu, F. Gumpert, J. Lohbreier, P.-O. Morin, V. Vohra, Y. Liu, Y. Zhou, C. J. Brabec, H.-J. Egelhaaf and A. Distler, *Joule*, 2024, **8**(4), 970–978.
10 J. Guo and J. Min, *Adv. Energy Mater.*, 2019, **9**, 1802521.
11 F. Machui, M. Hösel, N. Li, G. D. Spyropoulos, T. Ameri, R. R. Søndergaard, M. Jørgensen, A. Scheel, D. Gaiser and K. Kreul, *Energy Environ. Sci.*, 2014, **7**, 2792–2802.
12 A. Distler, C. J. Brabec and H. J. Egelhaaf, *Prog. Photovoltaics Res. Appl.*, 2021, **29**, 24–31.
13 G. Bernardo, T. Lopes, D. G. Lidzey and A. Mendes, *Adv. Energy Mater.*, 2021, **11**, 2100342.
14 L. Duan and A. Uddin, *Adv. Sci.*, 2020, **7**, 1903259.
15 X. Du, T. Heumueller, W. Gruber, A. Classen, T. Unruh, N. Li and C. J. Brabec, *Joule*, 2019, **3**, 215–226.
16 Y. Han, H. Dong, W. Pan, B. Liu, X. Chen, R. Huang, Z. Li, F. Li, Q. Luo and J. Zhang, *ACS Appl. Mater. Interfaces*, 2021, **13**, 17869–17881.
17 Q. Burlingame, M. Ball and Y.-L. Loo, *Nat. Energy*, 2020, **5**, 947–949.
18 S. A. Gevorgyan, M. V. Madsen, B. Roth, M. Corazza, M. Hösel, R. R. Søndergaard, M. Jørgensen and F. C. Krebs, *Adv. Energy Mater.*, 2016, **6**, 1501208.
19 I. A. Channa, A. Distler, B. Scharfe, S. Feroze, K. Forberich, B. Lipovšek, C. J. Brabec and H.-J. Egelhaaf, *Flexible Printed Electron.*, 2021, **6**, 025006.
20 M. Riede, D. Spoltore and K. Leo, *Adv. Energy Mater.*, 2021, **11**, 2002653.
21 E. N. Güler, A. Distler, R. Basu, C. J. Brabec and H.-J. Egelhaaf, *Flexible Printed Electron.*, 2022, **7**, 025003.
22 E. Pulli, E. Rozzi and F. Bella, *Energy Convers. Manage.*, 2020, **219**, 112982.
23 A. Anctil, E. Lee and R. R. Lunt, *Appl. Energy*, 2020, **261**, 114429.
24 P. Heinstein, C. Ballif and L.-E. Perret-Aebi, *Green*, 2013, **3**, 125–156.
25 J. Kettle, N. Bristow, T. K. Sweet, N. Jenkins, G. A. dos Reis Benatto, M. Jørgensen and F. C. Krebs, *Energy Environ. Sci.*, 2015, **8**, 3266–3273.
26 **https://www.gminsights.com/industry-analysis/polymer-solar-cells-market**.
27 S. Liu, D. Zhang, H.-J. Egelhaaf, G. Wang, X. Li, T. Heumüller, C. J. Brabec and N. Li, *J. Mater. Chem. A*, 2024, **12**(24), 14688–14697.
28 H.-J. Egelhaaf, F. Hoga, C. Brabec, A. Distler, M. Wagner, A. Dentel, G. Kießling, S. Feroze, S. Bordin and K. Senguttuvan, *BWK*, 2021, **73**, 16–21.
29 G. Bardizza, E. Salis, C. Toledo and E. D. Dunlop, *Prog. Photovoltaics Res. Appl.*, 2020, **28**, 593–600.
30 G. Dennler, K. Forberich, M. C. Scharber, C. J. Brabec, I. Tomiš, K. Hingerl and T. Fromherz, *J. Appl. Phys.*, 2007, **102**, 054516.
31 E. Magadley, R. Kabha and I. Yehia, *Renewable Energy*, 2021, **173**, 721–732.
32 V. Stoichkov, T. Sweet, N. Jenkins and J. Kettle, *Sol. Energy Mater. Sol. Cells*, 2019, **191**, 356–364.
33 S. Feroze, A. Distler, K. Forberich, I. A. Channa, B. Doll, C. J. Brabec and H.-J. Egelhaaf, *Sol. Energy*, 2023, **263**, 111894.
34 M. O. Reese, S. A. Gevorgyan, M. Jørgensen, E. Bundgaard, S. R. Kurtz, D. S. Ginley, D. C. Olson, M. T. Lloyd, P. Morvillo and E. A. Katz, *Sol. Energy Mater. Sol. Cells*, 2011, **95**, 1253–1267.
35 N. Gasparini, M. Salvador, S. Strohm, T. Heumueller, I. Levchuk, A. Wadsworth, J. H. Bannock, J. C. de Mello, H. J. Egelhaaf and D. Baran, *Adv. Energy Mater.*, 2017, **7**, 1700770.
36 S. Holliday, R. S. Ashraf, A. Wadsworth, D. Baran, S. A. Yousaf, C. B. Nielsen, C.-H. Tan, S. D. Dimitrov, Z. Shang and N. Gasparini, *Nat. Commun.*, 2016, **7**, 1–11.
37 S. Strohm, F. Machui, S. Langner, P. Kubis, N. Gasparini, M. Salvador, I. McCulloch, H.-J. Egelhaaf and C. Brabec, *Energy Environ. Sci.*, 2018, **11**, 2225–2234.
38 M. Wagner, A. Distler, V. M. Le Corre, S. Zapf, B. Baydar, H.-D. Schmidt, M. Heyder, K. Forberich, L. Lüer and C. J. Brabec, *Energy Environ. Sci.*, 2023, **16**, 5454–5463.
39 K. C. Tam, H. Saito, P. Maisch, K. Forberich, S. Feroze, Y. Hisaeda, C. J. Brabec and H.-J. Egelhaaf, *Sol. RRL*, 2022, **6**, 2100887.
40 Z. Jiang, S. Soltanian, B. Gholamkhass, A. Aljaafari and P. Servati, *RSC Adv.*, 2018, **8**, 36542–36548.
41 J. Luke, L. Corrêa, J. Rodrigues, J. Martins, M. Daboczi, D. Bagnis and J. S. Kim, *Adv. Energy Mater.*, 2021, **11**, 2003405.
42 Y. Han, J. Guo, Q. Luo and C.-Q. Ma, *Adv. Energy Sustainability Res.*, 2023, **4**, 2200179.
43 J. Balenzategui and F. Chenlo, *Sol. Energy Mater. Sol. Cells*, 2005, **86**, 53–83.

44 I. Geisemeyer, N. Tucher, B. Müller, H. Steinkemper, J. Hohl-Ebinger, M. C. Schubert and W. Warta, *IEEE J. Photovolt.*, 2016, **7**, 19–24.
45 I. Riedel, J. Parisi, V. Dyakonov, L. Lutsen, D. Vanderzande and J. C. Hummelen, *Adv. Funct. Mater.*, 2004, **14**, 38–44.
46 B. Ebenhoch, S. A. Thomson, K. Genevičius, G. Juška and I. D. Samuel, *Org. Electron.*, 2015, **22**, 62–68.
47 M. Hartner, A. Ortner, A. Hiesl and R. Haas, *Appl. Energy*, 2015, **160**, 94–107.
48 A. Karl, A. Osvet, A. Vetter, P. Maisch, N. Li, H. J. Egelhaaf and C. J. Brabec, *Prog. Photovoltaics Res. Appl.*, 2019, **27**, 460–468.
49 Y. Li, T. Li and Y. Lin, *Mater. Chem. Front.*, 2021, **5**, 2907–2930.
50 L. Duan, Y. Zhang, M. He, R. Deng, H. Yi, Q. Wei, Y. Zou and A. Uddin, *ACS Appl. Mater. Interfaces*, 2020, **12**, 27433–27442.
51 D. Chemisana, A. Moreno, M. Polo, C. Aranda, A. Riverola, E. Ortega, C. Lamnatou, A. Domènech, G. Blanco and A. Cot, *Renewable Energy*, 2019, **137**, 177–188.
52 H. Hintz, C. Sessler, H. Peisert, H.-J. Egelhaaf and T. Chassé, *Chem. Mater.*, 2012, **24**, 2739–2743.
53 P. Weitz, V. M. Le Corre, X. Du, K. Forberich, C. Deibel, C. J. Brabec and T. Heumüller, *Adv. Energy Mater.*, 2023, **13**, 2202564.
54 W. Greenbank, N. Djeddaoui, E. Destouesse, J. Lamminaho, M. Prete, L. Boukezzi, T. Ebel, L. Bessissa, H.-G. Rubahn and V. Turkovic, *Energy Technol.*, 2020, **8**, 2000295.

